Supplementary Information

Cuffless Wearable Sphygmomanometers using Dual Digital Optical Frequency Combs in Chalcogenide Chips

Ruifeng Zhong[1, +], Jingshun Pan[2, +], Qiang Li[1], Luya Li[1], Yi Xu[1], Zhihao Fu[1], Shuixian Yang[1], Changyuan Yu[3,4], Chao Lu[3,4, *], Xuming Zhang[3,5, *] & Zhaohui Li[1,6,*]

[1] School of Electronics and Information Technology, Guangdong Provincial Key Laboratory of Optoelectronic Information Processing Chips and Systems, Sun Yat-sen University, Guangzhou 510275, China.

[2] School of Information and Optoelectronic Science and Engineering, Guangdong Provincial Key Laboratory of Nanophotonic Functional Materials and Devices, South China Normal University, Guangzhou 510006, China.

[3] Photonics Research Institute, The Hong Kong Polytechnic University, Hong Kong, China.

[4] Department of Electronic and Information Engineering, The Hong Kong Polytechnic University, Hong Kong, China.

[5] Department of Applied Physics, The Hong Kong Polytechnic University, Hong Kong, China.

[6] Southern Marine Science and Engineering Guangdong Laboratory (Zhuhai), Zhuhai 519000, China.

[+] These authors contributed equally: Ruifeng Zhong, Jingshun Pan.

* Corresponding authors: enluchao@polyu.edu.hk, apzhang@polyu.edu.hk, lzhh88@mail.sysu.edu.cn

Table of Contents:

S1. Comparison of pulse pressure sensors

Various pressure sensors have been developed for human pulse wave monitoring based on piezoresistive[1-3], capacitive[4-6], piezoelectric[7-8], and optical[9] effects. Table S1 summarizes a few representative pulse sensors and compares them with our chalcogenide sensor. Here, we need to analyze the blood pressure using the combination of the wave velocity method and the characteristic parameter method. Therefore, the sensor needs both a high sensitivity and a fast response to ensure accurate and stable measurement in practical applications.

Table S1: Comparison of our chalcogenide sensor with other blood pressure sensors

Type of sensor	Structure	Sensitivity of pressure	Detection limit	Response rate / Response time	Stability (cycles)	Reference
Piezoresistive	Wrinkle	2.71×10^{-4} Pa^{-1}	40 Pa	16.7 Hz / 60 ms	5,000	[1]
	Sandwich	28.9 Pa^{-1}	100 Pa	50 Hz / 20 ms	10,000	[2]
	Microsphere	0.111 Pa^{-1}	20 Pa	10 Hz / 100 ms	10,000	[3]
Capacitive	Micropyramid	8.4 Pa^{-1}	30 Pa	>100 Hz / <10 ms	>15,000	[4]
	Sandwich	1.9 Pa^{-1}	10 Pa	> 10 Hz / <100 ms	1,000	[5]
	Sandwich	6.03 Pa^{-1}	9 Pa	11.9 Hz / 84 ms	/	[6]
Piezoelectric	Interlocked	3.12 V/Pa	1.8 Pa	18.9 Hz / 53 ms	5,000	[7]
	Interlocked	35 mA/Pa	0.6 Pa	>5 Hz / <200 ms	5,000	[8]
Optical	FP fiber	213 uW/Pa	/	200 Hz / 5 ms	70,000	[9]
DDOFC	Microring	218 Hz/Pa	23 Pa	2,000 Hz / 0.5 ms	4.3×10^{7}	This work

Regarding the sensitivity, the reported sensors based on different physical effects have different units, and thus cannot be compared directly. For a fair comparison, we choose the detection limit as the benchmark. It can be seen from Table S1 that the piezoelectric sensors have the best detection limit (~ 1 Pa), and our chalcogenide sensor (23 Pa) is comparable to the piezoresistive sensors (20 – 100 Pa) and the capacitive sensors (9 – 30 Pa).

Regarding the response, the electrical sensors, including the piezoresistive, capacitive and piezoelectric types, are generally limited by the physical effects and difficult to get a high response rate. Here the response rate means the maximum frequency of pressure waves that the sensor can respond to. It is simply a reciprocal of the response time. From Table S1, their response rates are typically 5 – 100 Hz. In contrast, our chalcogenide sensor has a response rate of up to 2,000 Hz (see Supplementary Section 8.3 below), ~ 10 times faster. This makes it possible to capture the ultrafast transient details of the pulse pressure waves, which are inaccessible using other sensors.

From Table S1, it is seen that our chalcogenide sensor has much better stability than the others, which typically last for ~10,000 cycles. In contrast, our chalcogenide sensor was tested for 4.3×10^7 cycles but remained stable in both frequency response and amplitude response (see Supplementary Section 8.4 below), marking a drastic increase by 3 orders of magnitude.

S2. Comparison of optical frequency dual-comb systems

Table S2 lists a few representative optical comb systems with superior performances. According to the generation techniques, optical frequency combs can be roughly divided into three types: *mode/phase-locked laser*, *electro-optic*, and *Kerr microcavity*. The mode/phase-locked laser type is the initial platform for the generation of optical frequency comb[10,11]. It can generate high-power broadband optical frequency combs, but the tooth spacing is difficult to tune and the system is relatively complex. The electro-optic frequency comb adopts the electro-optic modulation and allows for flexible design of the comb tooth spacing and the deviation of dual-comb, but the system is very complex and requires a lot of electrical and optical devices[12-15]. The Kerr microcavity optical frequency comb exploits a single mode laser coupled with the microcavity to stimulate the nonlinear effect in the microcavity to generate the optical frequency comb, which has a wide spectrum, a good coherence and a high integration[16-18], but often has poor stability. In addition, the comb tooth interval is limited by the microcavity, and can not be flexibly tuned.

Table S2: Comparison of DDOFC with other dual-comb systems

Type	Generation system	Bandwidth	f	Δf	Linewidth	Application	Reference
Mode/Phase-locked combs	2Fibers, 2Pumps	40.25 THz	115 MHz	138.5 Hz	0.35 Hz	Sensing of trace molecules	[10]
	Few lenses	26 THz	932 MHz	216 Hz	13 kHz	Crystal absorption spectroscopy	[11]
Electro-optic combs	3EOMs, 1AOM, 1YDFA	30 GHz	2.55 GHz	150 MHz	< 50 kHz	Gas absorption spectroscopy	[12]
	2IMs, 2AOMs, 2EDFAs	240 GHz	400 MHz	20Hz	< 2 Hz	Optomechanical spectroscopy	[13]
	2EOMs, 2AOMs, 2EDFAs	1.33 THz	500 MHz	0.1 kHz	/	Photothermal spectroscopy	[14]
	2IMs, 4AOMs, 2AMs	25 GHz	500 MHz	1Hz	< 0.5Hz	Digital holography	[15]
Kerr microcombs	2Rings, 2Pumps	18 THz	99 GHz	490 MHz	/	Laser-based ranging	[16]
	2Rings, 2Pumps	42 THz	127 GHz	12.8 MHz	< 100 kHz	Mid-infrared spectroscopy	[17]
	1Ring, 2IMs, 3AOMs, 4EDFAs	19.3 GHz	55 MHz	80 kHz	/	Mid-infrared spectroscopy	[18]
DDOFC	1IM	2.5 GHz	5 MHz	5 kHz	0.77 Hz	Blood pressure	This work

EOM: Electro-Optic Modulator; AOM: Acousto-Optic Modulator; YDFA: Ytterbium Doped Fiber Amplifier; IM: Intensity Modulation; EDFA: Erbium Doped Fiber Amplifier; AM: Amplitude Modulation.

Our DDOFC enables the generation of dual optical combs simultaneously in a single optical link, unlike the previous dual optical frequency combs that need to generate dual optical combs in two separate optical links and then couple/combine them into one optical link[14-18]. Therefore, our new DDOFC method has favourable features such as flexibility (like the electro-optic type) and simplicity (like the Kerr microcavity type). Here, to trade off between the comb interval and the beat frequency of the dual-comb, we choose the comb interval of 5 MHz and the beat frequency difference of 5 kHz.

S3. Fabrication of chalcogenide sensors

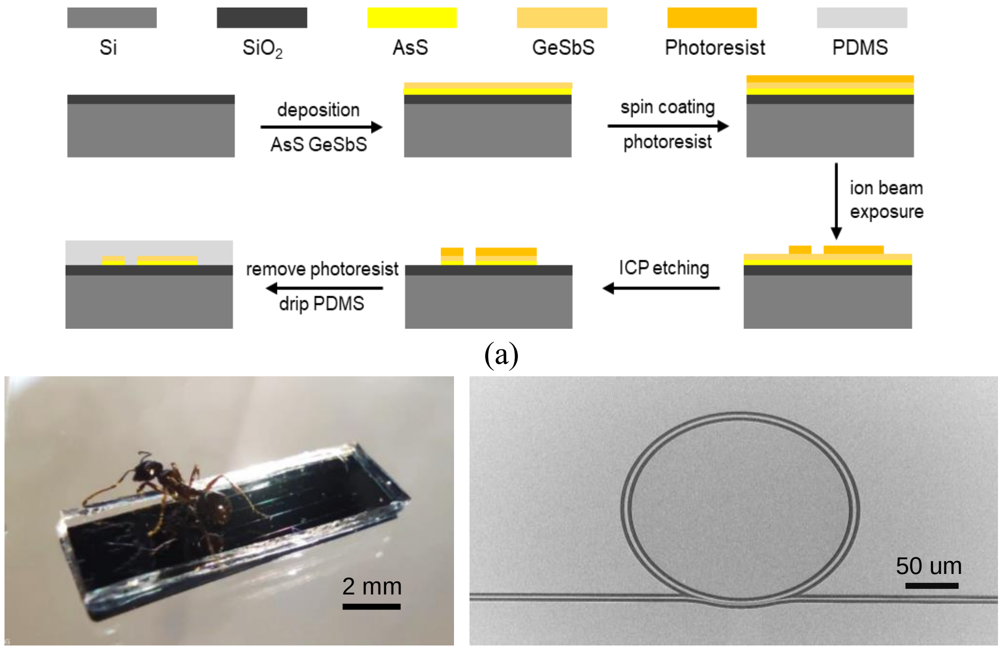

Figure S1: Device fabrication. (a) Fabrication process flow. The chalcogenide sensor devices by spin coating, photopatterning and ICP etching. (b) Photo of fabricated device, in which an ant is added to indicate the size difference. (c) SEM of a microring.

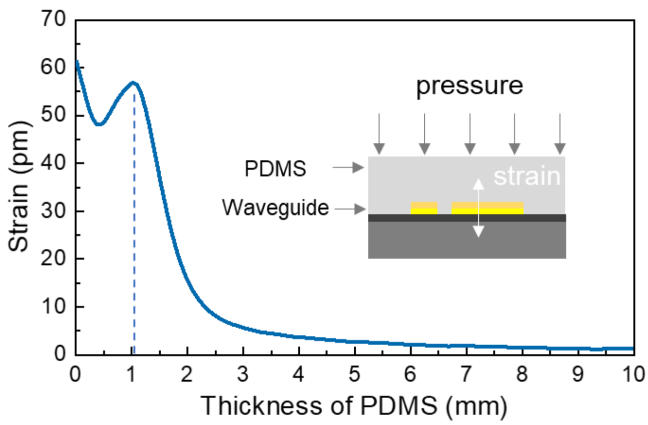

Figure S2: Simulated mechanical transmission effect as a function of the PDMS thicknesses. When pressure is applied on one surface of a PDMS layer (see the inset), the resulting strain on the surface of the opposite side goes down quickly with the increase in the thickness of the PDMS layer, but shows a peak when the PDMS thickness is about 1 mm.

S4. Selection and design of PDMS cover layer

Polydimethylsiloxane (PDMS) is a polymer material known for its optical transparency, elasticity, non-toxicity and biocompatibility, and provides a suitable option for chip encapsulation, particularly in applications that require soft contact with biological skins. Covering a PDMS layer onto a photon chip could yield multiple advantages. First, it protects micro/nano-structures on the chip from external disturbances such as dust, humidity and scratches, ensuring the long-term durability of the device. Second, its non-toxicity and biocompatibility ensure bio-safety for direct contact with human skin. Finally, its excellent elasticity and flexibility enable a conformal and tight fit with human skin, making it an ideal material for stress conduction[19,20].

Considering that the thickness of PDMS may affect the conduction of pressure, we simulated the effect of pulse pressure on device strain, and studied the mechanical conduction characteristics of PDMS with different thicknesses through finite element analysis, as shown in Fig. S2. As a general trend, the strain at the position of microring reduces quickly with the increase of PDMS thickness. Interestingly, the strain shows a peak at the thickness of ~ 1 mm, resulting in a good mechanical conductivity and a large deformation of the microring. Moreover, this thickness provides a good fit for the skin. Therefore, we chose 1 mm as the PDMS thickness.

In fabrication, the PDMS used a base and a curing agent (Dow-corning, GZJ-184) mixed in a 10:1 ratio. The prepared PDMS liquid of ~1 mm thick was drop-cast onto the photonic chip, and then it was cured in an oven at 120 °C for 2 h.

S5. Fiber coupling of bus waveguide

Here we will describe how to design a taper at the end of a bus waveguide for efficient optical coupling with an optical fiber, and then how to package the optical fiber with the device.

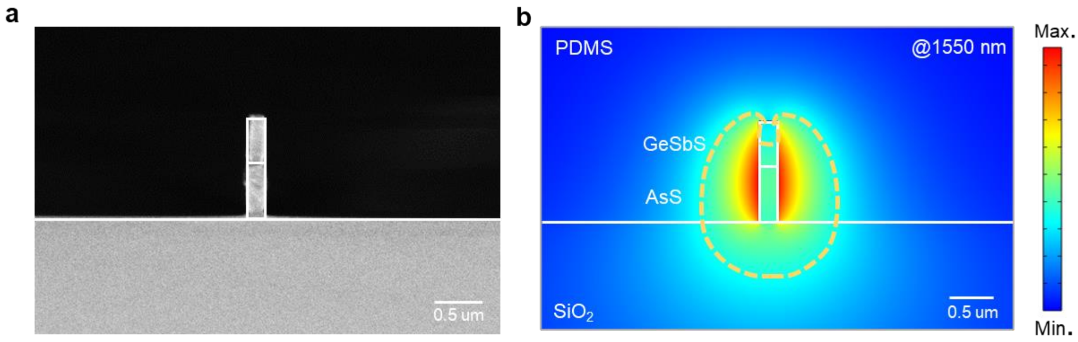

Figure S3: Tapered end of the bus waveguide. (a) SEM of the end of bus waveguide; and (b) simulated mode field distribution at 1,550 nm.

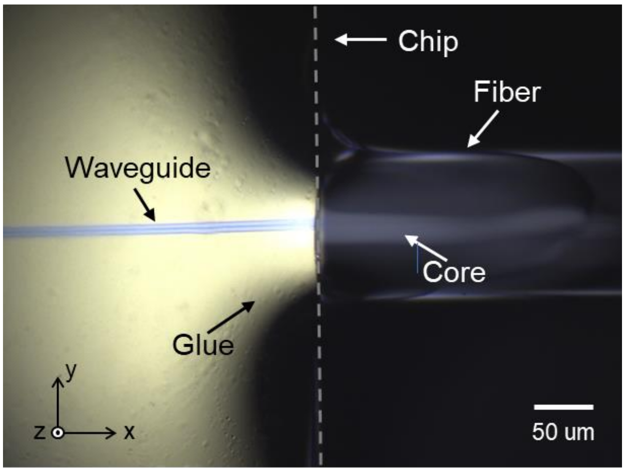

Figure S4: Microscopic image of the fiber-to-waveguide coupling and bonding. The glue (i.e., optical adhesive) is used to bond the optical fiber to the chalcogenide chip.

S5.1 Inverse taper design for the edge of waveguide

We adopted the edge coupling mode due to the advantages of small size and high coupling efficiency[21] and designed an inverse taper at the end of the bus waveguide to enhance coupling efficiency. Over a length of 1 mm, the waveguide end is tapered from

1,300 nm wide to 180 nm, and thus gradually looses the confinement of the optical mode field. Fig. S3 shows the SEM image and the simulated optical mode field of the end of taper. The yellow dashed line in Fig. S3b sketches the region of the mode field in which the intensity is reduced to $1/e^2$. It is seen that the optical mode field area is widened to ensure better matching of the optical mode field of the fiber.

S5.2 Procedures of fiber coupling and bonding

To couple and bond the optical fibers to the bus waveguide of the sensor chip, the sensor chip was positioned on the micropositioner platform and monitored under a microscope. The magnifications of the objective and the eyepiece were set to 12× and 20×, respectively. Based on the shape and size of the internal propagation mode of the bus waveguide, we opted for a single-mode fiber with a mode field diameter of 3.2 ± 0.3 μm at 1,550 nm (Nufern UHNA7, Coherent). With the visualization of the microscope, the tapered end of the bus waveguide was first roughly aligned with the single-mode fiber as illustrated in Fig. S4. This alignment was achieved by adjusting a three-axis high-precision translation stage (MAX311D/M, Thorlabs) beneath the fiber. It is worth noting that a small gap was left between the waveguide and the optical fiber for subsequent fine-tuning.

Next, the input side of the optical fiber was connected to a continuous-wave laser (Keysight, 8164B, 10 kHz linewidth, 1,550 nm), while the output side of the optical fiber was connected to an optical powermeter (PM100D, Thorlabs). Two three-axis stages supporting the two fibers were adjusted separately. After gradually reducing the gap between the fiber and the waveguide along the *x* direction, we carefully adjusted the fiber end along the *y* and *z* directions until the powermeter reading was maximized. Then, a small amount of UV-curable adhesive (NOA61, Norland) with a refractive index of 1.56 was dispensed at the connection point, followed by a UV curing step using a UV-curing lamp (NVSUA U365nm, Nichia) with a wavelength of 365 nm and an irradiation spot diameter of 1.5 mm. After several trials, we found the optimal curing conditions to be 5 min for the illumination time and 5 cm for the illumination distance. Finally, we got an integrated sensor device, in which a chalcogenide chip is coupled and bonded with two optical fibers for easy operation and testing.

S6. Theoretical analysis and design of chalcogenide chips

S6.1 Theoretical analysis of temperature compensation

Chalcogenide compounds are a class of compound materials with diverse compositions, and the variations in their components may result in positive or negative thermal-optic coefficients, which can be utilized to achieve an extremely low effective thermal-optic coefficient in the chalcogenide-based composite structures and devices in this study. Furthermore, chalcogenide materials have large photoelastic coefficients and low Young's modulus[22,23], making them ideal for high-sensitivity pressure sensing without requiring specialized structures[24]. This work employs the bi-layered composite film of $Ge_{25}Sb_{10}S_{65}$ (GeSbS) and $As_{20}S_{80}$ (AsS) to make the microrings and the bus waveguide. The substrate is SiO_2, and the cover layer is PDMS (Fig. 2b). Consequently, the effective refractive index of microrings and waveguide can be expressed as

$$n_{eff} = \Gamma_{GeSbS} n_{GeSbS} + \Gamma_{AsS} n_{AsS} + \Gamma_{SiO_2} n_{SiO_2} + \Gamma_{PDMS} n_{PDMS} \tag{S1}$$

here Γ_{GeSbS}, Γ_{AsS}, Γ_{SiO_2}, and Γ_{PDMS} are the spatial distributions of the mode field energy in the GeSbS layer, the AsS layer, the substrate and the cover, respectively.

Accordingly, the effective thermal-optic coefficient can be expressed as the first derivative of the effective refractive index concerning temperature as written by

$$\frac{\partial n_{eff}}{\partial T} = \Gamma_{GeSbS} \frac{\partial n_{GeSbS}}{\partial T} + \Gamma_{AsS} \frac{\partial n_{AsS}}{\partial T} + \Gamma_{SiO_2} \frac{\partial n_{SiO_2}}{\partial T} + \Gamma_{PDMS} \frac{\partial n_{PDMS}}{\partial T} \tag{S2}$$

According to Eq. (S2), it is possible to achieve $\partial n_{eff}/\partial T = 0$ by properly designing the fill factors of the composite layers, leading to a complete temperature compensation for the sensor device to eliminate the influence of temperature change.

Referring to Fig. 2b, the refractive index of chalcogenide materials is relatively high (2.18 – 2.28) at 1,550 nm, resulting in a significant optical mode confinement within the regions of GeSbS and AsS. Consequently, the leakage of the optical mode to the substrate SiO_2 and the cover PDMS can be neglected, allowing for a further simplification of Eq. (S2) to the expression below,

$$\frac{\partial n_{eff}}{\partial T} = \Gamma_{GeSbS}\frac{\partial n_{GeSbS}}{\partial T} + \Gamma_{AsS}\frac{\partial n_{AsS}}{\partial T} \quad \text{(S3)}$$

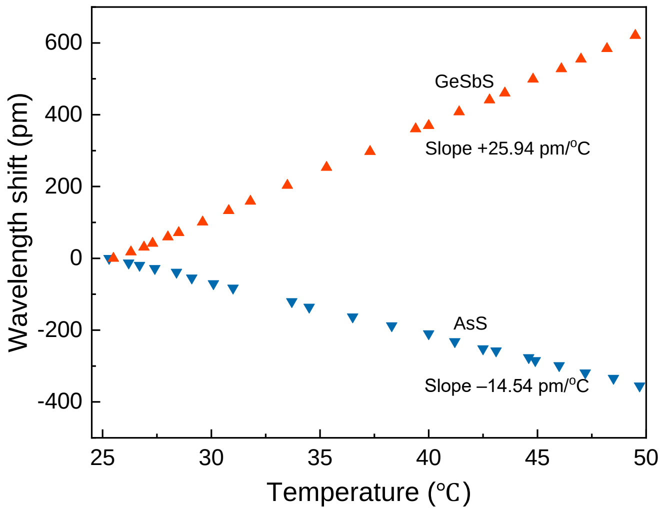

Figure S5 Measured temperature drifts of the microring resonators made of either only GeSbS or only AsS. With the temperature change, the resonant peaks of the microrings experience different trends of wavelength shifts. For GeSbS, the temperature drift is +25.94 pm/°C, whereas for AsS, it is -14.54 pm/°C. They have opposite signs but comparable magnitudes.

S6.2 Temperature drift of GeSbS and AsS

The chalcogenide materials exhibit remarkable diversity. Among them, GeSbS and AsS possess opposite thermal-optic coefficients[25,26]. Due to the difficulty in directly obtaining the temperature-dependent refractive index from the relationship between the refractive index change and the wavelength change[27], we conducted separate experiments on the temperature-dependent wavelength shift using the microring resonators made of either only GeSbS or only AsS. As a result, a temperature change would cause a shift of resonant peak wavelength. As shown in Fig. S5, the GeSbS microring resonator causes a linear increase of the wavelength shift in response to an increase in temperature from 25 to 50 ºC, whereas the AsS one results in a linear decrease. From the slopes of fit curves, we can obtain the temperature drift is +25.94 pm/ºC for GeSbS and -14.54 pm/ºC for AsS. They have opposite signs but comparable magnitudes. Therefore, it is possible to compensate for the temperature drift in the GeSbS/AsS composite waveguides by proper design of the optical field distributions.

S6.3 Simulation of mode field distribution and choice of GeSbS/AsS thicknesses

To achieve a thermal-optic coefficient $\partial n_{eff}/\partial T = 0$, the ratio of the energy distributions of mode fields in the GeSbS region and the AsS region should be inversely proportional to the ratio of their temperature drifts given by Fig. S5. It is worth noting that the energy distribution of the optical mode field in the waveguide is dependent on the wavelength as well, though slightly[27]. Our simulations find that the energy portion in the AsS layer shows an increasing trend for longer wavelengths. Concerning the GeSbS/AsS waveguides, since the AsS has a negative temperature drift (i.e., -14.54 pm/ºC), more energy in the AsS layer would cause a negative temperature drift for the whole GeSbS/AsS waveguide, which is consistent with the $\Delta\lambda/\Delta T$ curve in Fig. 2c. This implies that the temperature compensation effect is wavelength dependent but the influence is minimal. Consequently, we can achieve an excellent temperature compensation over the wavelength range of 1,500 to 1,590 nm. Given the total thickness of GeSbS/AsS waveguide to be 1 μm, we simulated various thickness ratios of GeSbS to AsS as plotted in Fig. S6.

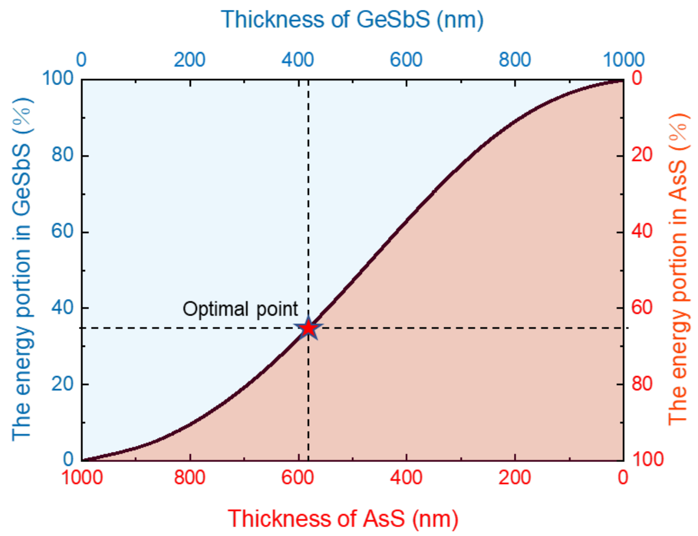

Figure S6: Choice of thicknesses of the GeSbS layer and the AsS layer in the GeSbS/AsS composite structure with a total thickness of 1 μm. The *y* axes represent the portions of optical mode field energies in the GeSbS layer and the AsS layer, respectively.

According to Eq. (S3), for $\partial n_{eff}/\partial T = 0$, it is necessary to have

$$\Gamma_{GeSbS}/\Gamma_{AsS} = (\partial n_{AsS}/\partial T)/(\partial n_{GeSbS}/\partial T). \quad \text{(S4)}$$

Using the measured temperature drifts for GeSbS and AsS in Fig. S5, we can get $\Gamma_{GeSbS} = 35.9\%$ and $\Gamma_{AsS} = 64.1\%$, as indicated by the star sign in Fig. S6. When the GeSbS/AsS waveguide is set to have a thickness of 1 μm, we can obtain the thicknesses of GeSbS and AsS to be 425 nm and 575 nm, respectively. These are used as the optimal design parameters of the GeSbS/AsS waveguide in this work. In experiments, the fabricated GeSbS/AsS microring resonators show a temperature drift of only 0.012 pm/ºC at 1,550 nm, and the magnitude of temperature drift < 0.5 pm/°C over the whole range of 1,500 – 1,590 nm, as shown in Fig. 2c.

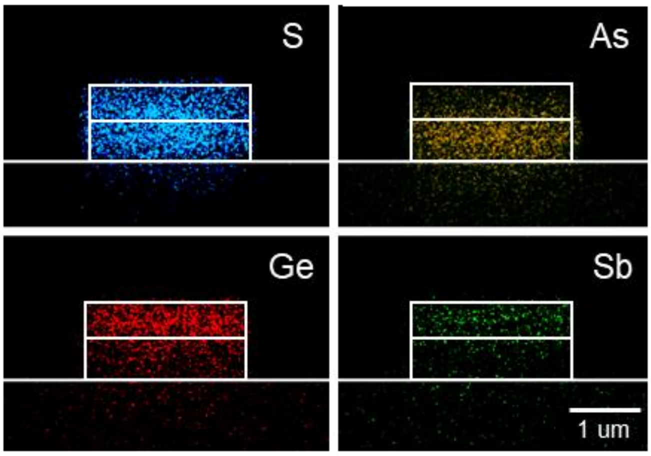

Figure S7: Elemental mappings of GeSbS/AsS waveguide. The S element distributes over the whole cross-section, As mostly in the lower part (i.e., the AsS layer), while Ge and Sb are mostly in the upper part (i.e., the GeSbS layer). Diffusion to undesired regions is observable due to the fabrication process, but it is little and thus has negligible influence on the waveguide properties.

S7. Elemental mappings of GeSbS/AsS waveguide's cross-section

To verify the waveguide is indeed composed of two designed materials (i.e., GeSbS and AsS), we used an electric refrigeration energy-dispersive X-ray spectroscope (Oxford Ultim Max40 EDS) to measure the distribution of elemental components as shown in Fig. S7. It can be seen that the S element is distributed in the whole waveguide cross-section. This is reasonable since both GeSbS and AsS contain S element. In contrast, the As element is mostly distributed in the lower layer of the waveguide, while Ge and Sb are mostly distributed in the upper layer of the waveguide. These agree well with our material choices and fabrication. Nevertheless, it is observable that some As is in the upper layer and some Ge and Sb in the lower layer. This is due to the diffusion in the fabrication process. Fortunately, the diffusion is low and has little impact on the waveguide performance.

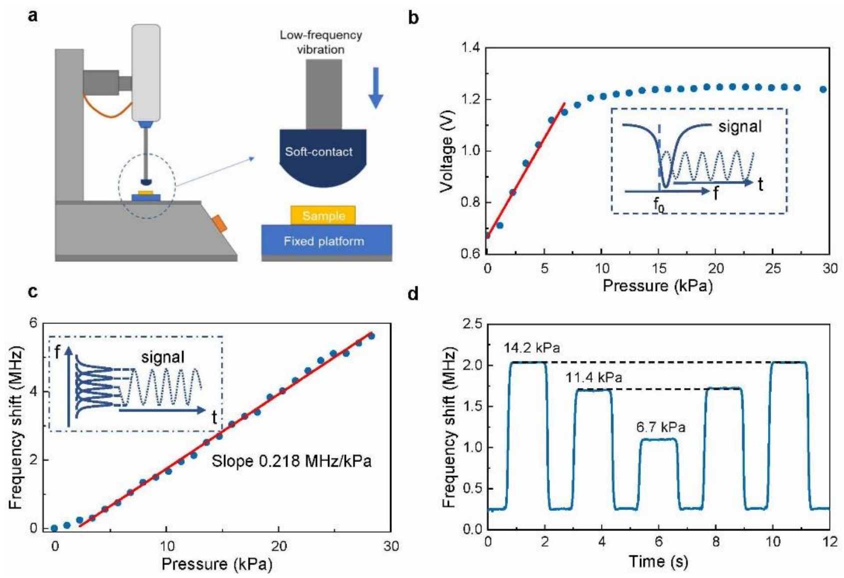

Figure S8: Device characterization. (a) Diagram of experimental setup. Measured responses using (b) the wavelength-locked detection and (c) the DDOFC method. (d) Repeatability tests under different pressures.

S8. Device characterization

S8.1 Test setup

We characterized the performance of the chalcogenide sensor using an experimental setup as shown in Fig. S8a. A pressure source was generated using an electric pressure calibrator (JSV-H1000) with a soft contact at the pressure interface. The chalcogenide sensor was placed directly below the pressure calibrator, and a motorized linear stage controlled the height position of the soft contact to make contact with the chalcogenide sensor. In the electric pressure calibrator, the standard pressure values were obtained from the feedback loop. For comparison, the responses of the chalcogenide were measured using two methods: the traditional *wavelength-locked method* and the new *DDOFC method*. The former uses a laser beam with a fixed wavelength aligned to one side of the envelope of the microring's transmission peak, and the output is measured by a photodetector. When the microring's transmission peak is shifted in response to the pressure, the transmitted intensity is varied and consequently, the output voltage of the photodetector is changed. In contrast, the latter utilizes the DDOFC for parallel interrogation of the pressure response in the two microrings of the chalcogenide chip (see Methods, the section "Generation and demodulation of DDOFC").

S8.2 Linear range & repeatability

The measured results by the wavelength-locked method and the DDOFC are plotted in Fig. S8b&c. It can be observed the wavelength-locked method has a limited linear range of only 0 – 1 kPa and then tends to saturate (Fig. S8b); nevertheless, the DDOFC method presents a much wider linear range of 0 – 50 kPa, with a sensitivity of 0.218 MHz/kPa (i.e., 218 Hz/Pa, see Fig. S8c). This is because the linear range of DDOFC is determined by the bandwidth of DDOFC while that of the wavelength-locked method is limited by the half-width of the microring resonance. We also quantified the repeatability and response of the chalcogenide sensor by applying different pressures repeatedly. As shown in Fig. S8d, when the pressure is reduced from 14.2 kPa to 11.4 kPa and further to 6.7 kPa, and then increased back to 11.4 kPa and 14.2 kPa successively, the magnitudes of frequency shift response well repeat themselves. This qualitatively verifies the high repeatability of the chalcogenide sensor device.

S8.3 Dynamic response

The response speed of the sensor is of high importance to the detection of blood pulse waves in the temporal domain. To measure the sensor's response time, we gently tapped the chalcogenide sensor with a pair of tweezers and captured the response as shown in Fig. S9. The rise time and the fall time are both ~0.5 ms. Correspondingly, the maximum response rate can be 2,000 Hz, enabling to capture the previously inaccessible transient details of the pulse pressure waves. It is worth noting that the sampling rate of our DDOFC system is 5 kHz (corresponding to 0.2 ms), fast enough to sample the pulse waveforms (~ 1 ms). In other words, the DDOFC chalcogenide sensor has a fast response and a high-resolution sampling rate for the detection of blood pulse waves.

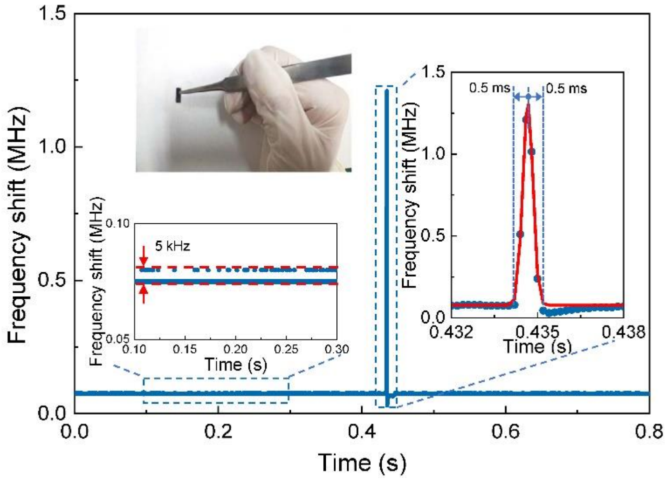

Figure S9: Dynamic response. The device shows a clear peak in response to a gentle tapping by tweezers. The inset on the left shows the noise level of the device is only 5 kHz. The inset on the right shows a magnified view of the response, in which blue dots represent experiment data and the red line shows the Gaussian fitting. It shows the rise time and the fall time are both 0.5 ms.

S8.4 Detection limit

Based on the data displayed in the left inset of Figure S9, the device exhibits an intrinsic noise level below 5 kHz without external forces. This noise level may originate from the linewidth of the laser (100 Hz) and the thermal noise of the detector. With the sensitivity calibration of the DDOFC device as 218 Hz/Pa, as shown in Figure S8c, the detection limit can be calculated as 23 Pa through dividing the noise level by the sensitivity of the device.

S8.5 Long-term stability

Subsequently, we validated the long-term stability of the chalcogenide sensor by using a high-frequency piezoelectric transducer to generate the pressure source. We drove the transducer with an AC signal (3 V, 500 Hz) from a signal generator. The vibration plate of the piezoelectric transducer was attached to the PDMS surface of the chalcogenide sensor. The long-term stability can be characterized in two aspects: *how many cycles* or *how long* the device can be operated without notable performance degradation.

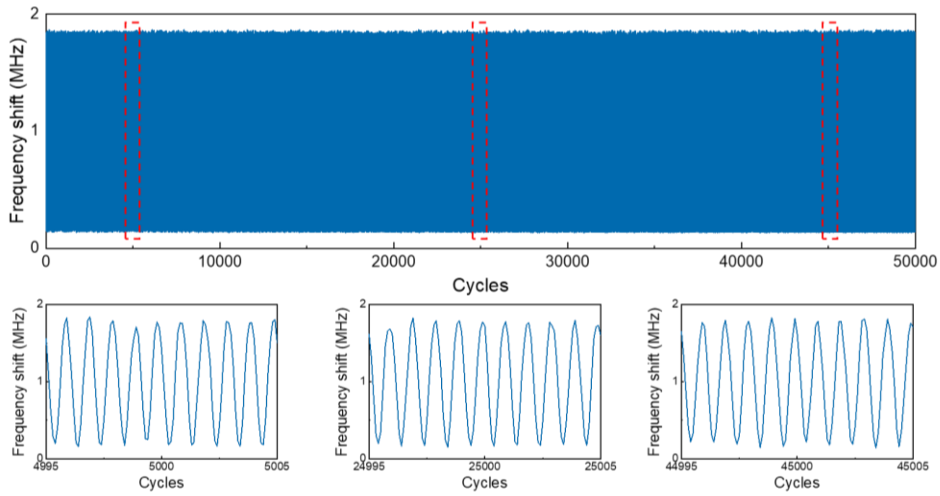

Figure S10: Device long-term stability test for 50,000 cycles. A piezoelectric transducer is used to generate the 500-Hz pressure waves. The enlarged views sampled from the beginning, the middle and the end all show stable waveforms.

To examine the stability in terms of the number of cycles, we tried 50,000 cycles of repetitive signals as shown in the upper panel of Fig. S10. Enlarged views of the beginning, middle, and end segments show stable curves (the lower panel of Fig. S10), well demonstrating the excellent stability of the chalcogenide sensor. It is noted that 50,000 cycles correspond to a duration of only 100 s using the piezoelectric transducer, but ~ 12 h for human blood pulses (assuming a heart rate of 70 beats/min). Besides, the number of 50,000 cycles is not the limit of stable operation. Surely the chalcogenide sensor can run for many more cycles.

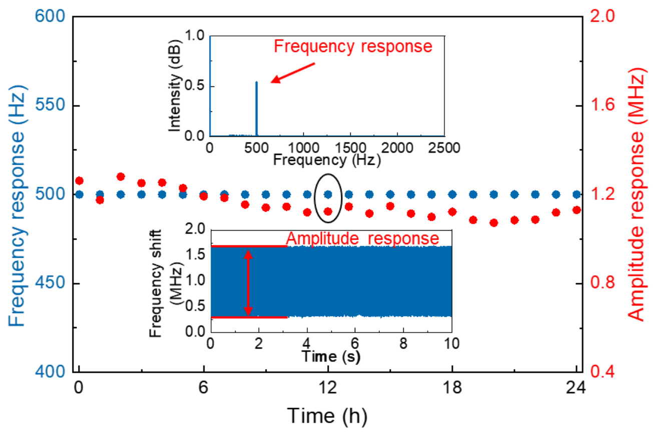

Figure S11: Device long-term stability test of continuous operation for 24 hours. The blue dots represent the frequency of response signals, whereas the red dots indicate the magnitude of response signals. The upper inset plots the power spectrum of measured signals, showing only a line of 500 Hz, the same as that of the pressure source. The lower inset exemplifies the sampled response waves in a window of 10 seconds.

To examine the stability in terms of the time, we conducted a continuous operation of the chalcogenide sensor for 24 hours. Similarly, we drove a piezoelectric transducer with a sinusoidal signal (amplitude 3 V, frequency 500 Hz) to provide the pressure wave source. The test results are shown in Fig. S11. Due to the overwhelming amount of data collected continuously in 24 hours, we chose only 10 seconds of every hour for easy analysis in two aspects: frequency response stability and amplitude response stability.

As shown by the blue dots and the upper inset of Fig. S11, the frequency of the sensor response is very stable, maintaining almost no change at 500 Hz. Regarding the amplitude response (the red dots and the lower inset in Fig. S11), it presents a small variation of only ±3.6%, which is negligible in practical blood pressure monitoring. It is noted that the 24-hour operation corresponds to 4.3×10^7 cycles of the pressure wave. Similarly, 4.3×10^7 cycles correspond to a duration of 1.2 years for human blood pulses (assuming a heart rate of 70 beats/min). And, the duration of 24 hours is not the limit of stable operation. Surely the chalcogenide sensor can be run much longer.

In summary, our chalcogenide sensor showed an ultra-stable frequency response and a negligible change of amplitude response over 24 h (equivalently, 4.3×10^7 cycles), well proving its potential for continuous monitoring of blood pressure over a long period.

S8.6 Estimation of temperature tolerance

To show the benefit of temperature compensation, here we will estimate the tolerance to working temperature. In the DDOFC, the two digital combs are distributed over a bandwidth of 2.5 GHz. As long as the frequency shift of the combs induced by the temperature change is within the bandwidth, the beat of two digital combs still holds, and thus the DDOFC detection method remains valid.

At 1550 nm, the bandwidth of 2.5 GHz corresponds to a wavelength range of 0.02 nm. Therefore, the maximum temperature range is

$$(0.02 \text{ nm})/(0.012 \text{ pm/}^{\circ}\text{C}) = 1{,}666\ ^{\circ}\text{C}.$$

This is large enough for the operation of sphygmomanometers directly in the environmental condition, which typically has a temperature range from -10 to +40 ºC, and in extreme cases, maybe from -100 to +100 ºC.

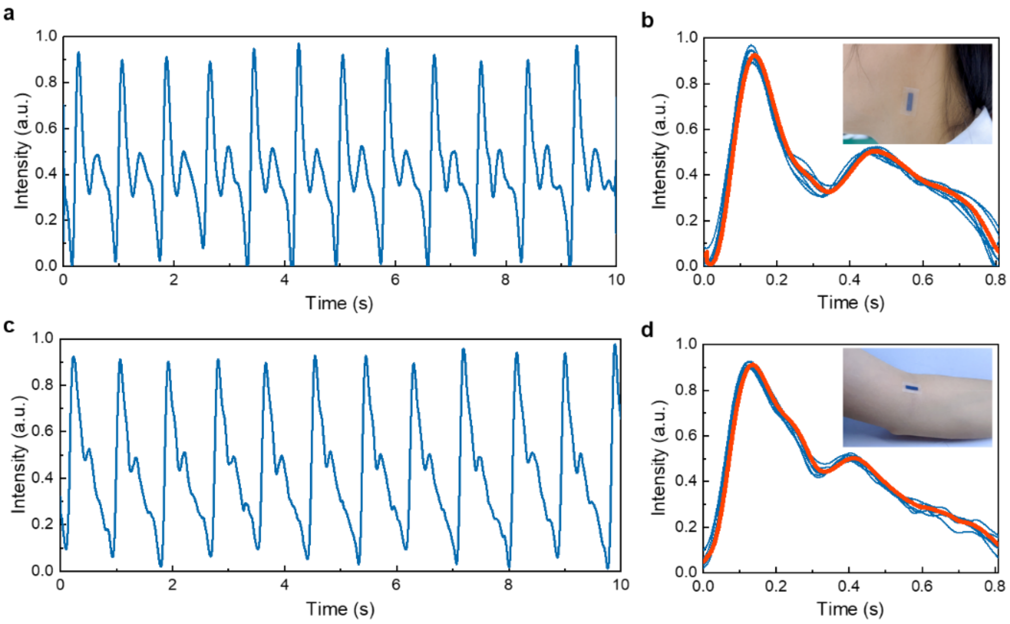

Figure S12: Experiments of continuous blood pressure monitoring on neck and antecubital fossa. (a) Continuous pulse wave and (b) average wave of the carotid artery. (c) Continuous pulse wave and (d) averaged wave of the brachial artery.

S9. Continuous monitoring of blood pulse waves at different body sites

To exemplify the broad application prospects of this research, we conducted further tests at different body sites. In addition to attaching the chalcogenide sensor to the wrist to capture the pulse waves of the radial artery as shown in Fig. 4, we pasted it onto the neck and the antecubital fossa (see the insets of Fig. S12b&d). The 10-second waveforms from the carotid and brachial arteries are displayed in Fig. S12a&c, respectively. And the averaged results are plotted in Fig. S12b&d. The red lines represent the averaged pulse waveform, while the blue lines show the raw data. It is easy to see that (1) the individual pulse waves exhibit a good consistency over a short period; and (2) the averaged waveforms and the associated characteristic points are different when measured at different body sites. These prominent features in the waveforms facilitate the accurate extraction and analysis of vital health information.

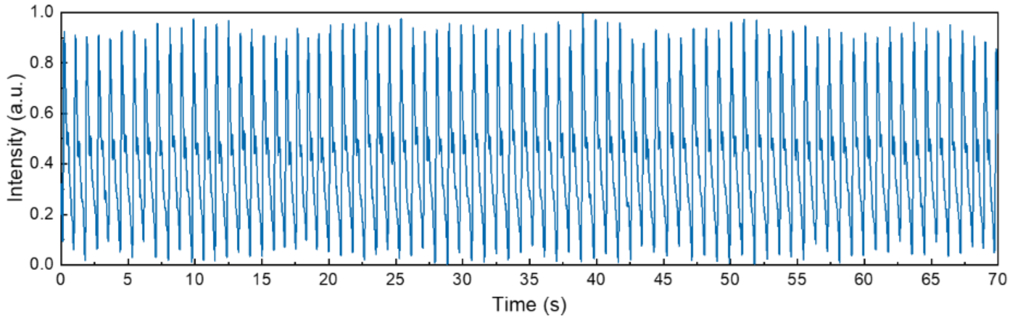

(a)

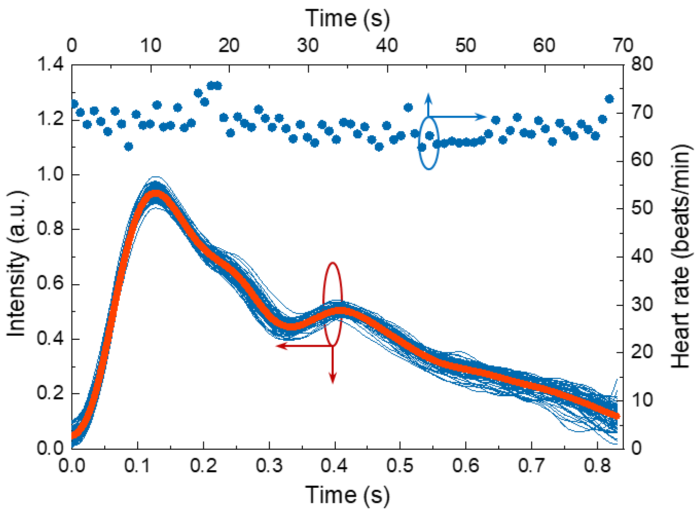

(b)

Figure S13: Demonstration of the stable operation of the chalcogenide sensor over a prolonged time. (a) Waveforms from the radial artery. (b) Characteristic curve of the radial artery (lines) and heart rate (dotted). In (a), the time span of only 70 s is shown so that each waveform is still visible. The measurement can be conducted for hours and even days.

In addition, for wearable devices, the capability for stable operation over a prolonged period on the human body is a crucial performance indicator as well. For further demonstration, we placed the chalcogenide sensor on the radial artery and captured the data continuously, as shown in Fig. S13a. The pulse cycles exhibited excellent stability. After the averaging and overlaying of several dozen sets of pulse cycles, the results are plotted in Fig. S13b. The red line represents the averaged pulse waveform, while the blue line represents the raw data. The characteristic points in the pulse wave are clear and distinct, showing excellent consistency and high precision in the pulse waves and indicating the sensor's high stability and sensitivity. Since heart rate is the reciprocal of the pulse cycle, the heart rate can be obtained by extracting the pulse wave cycle as plotted by blue dots in Fig. S13b. It is of high significance for continuous health monitoring as well.

The volunteer for the continuous blood pressure monitoring experiments experienced no harm or discomfort, and agreed with the publication of measured data.

S10. Analysis of the relationship between pulse waves and blood pressure

Pulse wave velocity (PWV) refers to the speed at which the pulse propagates along the blood vessels. Measuring PWV is a well-established classical method to determine the elasticity of large arteries, and it is generally considered the standard for evaluating the health of the cardiovascular system. PWV depends on the mechanical properties of the arterial wall (e.g., viscosity and elasticity), the geometry (e.g., diameter and wall thickness), and the blood density. Their relationship can be expressed by the Moens-Korteweg equation

$$v = \sqrt{\frac{gE\alpha}{\rho d}} \tag{S5}$$

where v represents the PWV, g is the acceleration due to travity, E is the elastic modulus of the blood vessel wall, ρ is the blood density, α is the thickness of the blood vessel wall, and d is the internal diameter of the blood vessel. The elastic modulus E is related to the blood pressure P by

$$E = E_0 e^{\gamma P} \tag{S6}$$

where E_0 is the elastic modulus at zero pressure, P is the blood pressure (mmHg), and γ is a parameter of the vascular property, typically treated as a constant. Then, the PWV can be expressed by

$$v = \frac{S}{T} \tag{S7}$$

where S denotes the propagation distance of pulse wave, and T is the pulse wave propagation time. The combination of Eqs. (S5) and (S6) with Eq. (S7) yields

$$P = \frac{1}{\gamma}\ln(\frac{\rho d S^2}{g\alpha E_0} - 2\ln T) \tag{S8}$$

Ignoring the changes in the artery's internal diameter d and the wall thickness α with the variation of blood pressure P, the first term on the right side of Eq. (S8) can be treated as a constant. By taking differentiation, we can get a simple expression as

$$\Delta P = -\frac{2}{\gamma T}\Delta T \tag{S9}$$

Therefore, the change of blood pressure ΔP is proportional to the change of pulse wave propagation time ΔT. For an individual, the elasticity of blood vessels does not undergo significant changes over a short period, making the variation in pulse wave propagation time an essential factor for assessing blood pressure conditions[28]. However, blood pressure is often a result of the combined effect of various factors. For example, when the pulse wave propagates from the heart to the arterial system, it is affected not only by the heart itself but also by various physiological factors such as vascular resistance, arterial wall elasticity, and blood viscosity at different levels of arteries and branches. This results in characteristic points in the pulse wave containing rich physiological and pathological information about the cardiovascular system, including blood pressure. To further enhance the accuracy of the analysis, the time information of characteristic points can be regressed together with the pulse wave propagation time ΔT[29].

Reference

1. Zhu, H., Luo, H., Cai, M.&Song, J. A Multifunctional Flexible Tactile Sensor Based on Resistive Effect for Simultaneous Sensing of Pressure and Temperature. *Adv. Sci.* e2307693 (2023).
2. Zhang, F., Zang, Y., Huang, D., Di, C. A.&Zhu, D. Flexible and self-powered temperature-pressure dual-parameter sensors using microstructure-frame-supported organic thermoelectric materials. *Nat.Commun.* **6,** 8356 (2015).
3. Xu, M.et al. Flexible pressure sensor using carbon nanotube-wrapped polydimethylsiloxane microspheres for tactile sensing. *Sens. Actuators,* **A 284,** 260-265 (2018).
4. Schwartz, G.et al. Flexible polymer transistors with high pressure sensitivity for application in electronic skin and health monitoring. *Nat.Commun.* **4,** 1859 (2013).
5. Liu, F.et al. An Omni-Healable and Highly Sensitive Capacitive Pressure Sensor with Microarray Structure. *Chemistry* **24**, 16823-16832 (2018).
6. Yi, Q.et al. A self-powered triboelectric MXene-based 3D-printed wearable physiological biosignal sensing system for on-demand, wireless, and real-time health monitoring. *Nano Energy* **101**, (2022).
7. Yang, T.et al. Hierarchically structured PVDF/ZnO core-shell nanofibers for self-powered physiological monitoring electronics. *Nano Energy* **72,** (2020).
8. Park, J., Kim, M., Lee, Y., Lee, H. S., & Ko, H. Fingertip skin–inspired microstructured ferroelectric skins discriminate static/dynamic pressure and temperature stimuli. *Sci. Adv.* **1,** e1500661 (2015).
9. Muraviev, A. V., Smolski, V. O., Loparo, Z. E.&Vodopyanov, K. L. Massively parallel sensing of trace molecules and their isotopologues with broadband

subharmonic mid-infrared frequency combs. *Nat. Photon.* **12,** 209-214 (2018).

10. Ideguchi, T., Nakamura, T., Kobayashi, Y.&Goda, K. Kerr-lens mode-locked bidirectional dual-comb ring laser for broadband dual-comb spectroscopy. *Optica* **3,** (2016).
11. Huang, D., Shi, Y., Li, F.&Wai, P. K. A. Fourier Domain Mode Locked Laser and Its Applications. *Sensors* **22,** (2022).
12. Long, D. A.et al. Nanosecond time-resolved dual-comb absorption spectroscopy. *Nat. Photon*. (2023).
13. Ren, X.et al. Dual-comb optomechanical spectroscopy. *Nat. Commun.* **14,** 5037 (2023).
14. Wang, Q.et al. Dual-comb photothermal spectroscopy. *Nat. Commun.* **13,** 2181 (2022).
15. Vicentini, E., Wang, Z., Van Gasse, K., Hänsch, T. W.&Picqué, N. Dual-comb hyperspectral digital holography. *Nat. Photon.* **15,** 890-894 (2021).
16. Lukashchuk, A., Riemensberger, J., Karpov, M., Liu, J.&Kippenberg, T. J. Dual chirped microcomb based parallel ranging at megapixel-line rates. *Nat. Commun.* **13,** 3280 (2022).
17. Yu, M.et al. Silicon-chip-based mid-infrared dual-comb spectroscopy. *Nat. Commun.* **9,** 1869 (2018).
18. Bao, C.et al. Architecture for microcomb-based GHz-mid-infrared dual-comb spectroscopy. *Nat. Commun.* **12,** 6573 (2021).
19. Luo, N.et al. Flexible Piezoresistive Sensor Patch Enabling Ultralow Power Cuffless Blood Pressure Measurement. *Adv. Funct. Mater.* **26,** 1178-1187 (2015).
20. Yi, Z.et al. Piezoelectric Dynamics of Arterial Pulse for Wearable Continuous Blood Pressure Monitoring. *Adv. Mater.* **34,** 2110291 (2022).

21. Marchetti, R., Lacava, C., Carroll, L., Gradkowski, K.&Minzioni, P. Coupling strategies for silicon photonics integrated chips. *Photonics Res.* **7,** 201-239 (2019).

22. Cao, Z., Dai, S., Ding, S., Liu, C.&Wu, J. Correlation between acousto-optic and structural properties of Ge–Sb–S chalcogenide glasses. *Ceram. Int.* **46,** 10385-10391 (2020).

23. Savchenko, N. D.et al. Calculation of elastic constants for $(GeS_2)_x(As_2S_3)_{1-x}$ glasses. *AIP Conf. Proc.* **963**, 1363-1366 (2007).

24. Pan, J.et al. Parallel interrogation of the chalcogenide-based micro-ring sensor array for photoacoustic tomography. *Nat. Commun.* **14,** 3250 (2023).

25. Xia, D.et al. Integrated Chalcogenide Photonics for Microresonator Soliton Combs. *Laser Photonics Rev.* **17,** 2200219 (2022).

26. Jean, P.et al. Sulfur-rich chalcogenide claddings for athermal and high-Q silicon microring resonators. *Opt. Mater. Express* **11,** 913-925 (2021).

27. He, L.et al. Broadband athermal waveguides and resonators for datacom and telecom applications. *Photonics Res.* **6,** 987-990 (2018).

28. Li, J.et al. Thin, soft, wearable system for continuous wireless monitoring of artery blood pressure. *Nat. Commun.* **14,** 5009 (2023).

29. Kireev, D.et al. Continuous cuffless monitoring of arterial blood pressure via graphene bioimpedance tattoos. *Nat. Nanotechnol.* **17,** 864-870 (2022).